

FULL PAPER

Open Access



Stochastic ground-motion simulations for the 2016 Kumamoto, Japan, earthquake

Long Zhang^{1,2*}, Guangqi Chen¹, Yanqiang Wu³ and Han Jiang⁴

Abstract:

On April 15, 2016, Kumamoto, Japan, was struck by a large earthquake sequence, leading to severe casualty and building damage. The stochastic finite-fault method based on a dynamic corner frequency has been applied to perform ground-motion simulations for the 2016 Kumamoto earthquake. There are 53 high-quality KiK-net stations available in the Kyushu region, and we employed records from all stations to determine region-specific source, path and site parameters. The calculated *S*-wave attenuation for the Kyushu region beneath the volcanic and non-volcanic areas can be expressed in the form of $Q_s = (85.5 \pm 1.5)f^{0.68 \pm 0.01}$ and $Q_s = (120 \pm 5)f^{0.64 \pm 0.05}$, respectively. The effects of lateral *S*-wave velocity and attenuation heterogeneities on the ground-motion simulations were investigated. Site amplifications were estimated using the corrected cross-spectral ratios technique. Zero-distance kappa filter was obtained to be the value of 0.0514 ± 0.0055 s, using the spectral decay method. The stress drop of the mainshock based on the USGS slip model was estimated optimally to have a value of 64 bars. Our finite-fault model with optimized parameters was validated through the good agreement of observations and simulations at all stations. The attenuation characteristics of the simulated peak ground accelerations were also successfully captured by the ground-motion prediction equations. Finally, the ground motions at two destructively damaged regions, Kumamoto Castle and Minami Aso village, were simulated. We conclude that the stochastic finite-fault method with well-determined parameters can reproduce the ground-motion characteristics of the 2016 Kumamoto earthquake in both the time and frequency domains. This work is necessary for seismic hazard assessment and mitigation.

Keywords: Ground-motion simulations, Stochastic finite-fault method, 2016 Kumamoto earthquake

Introduction

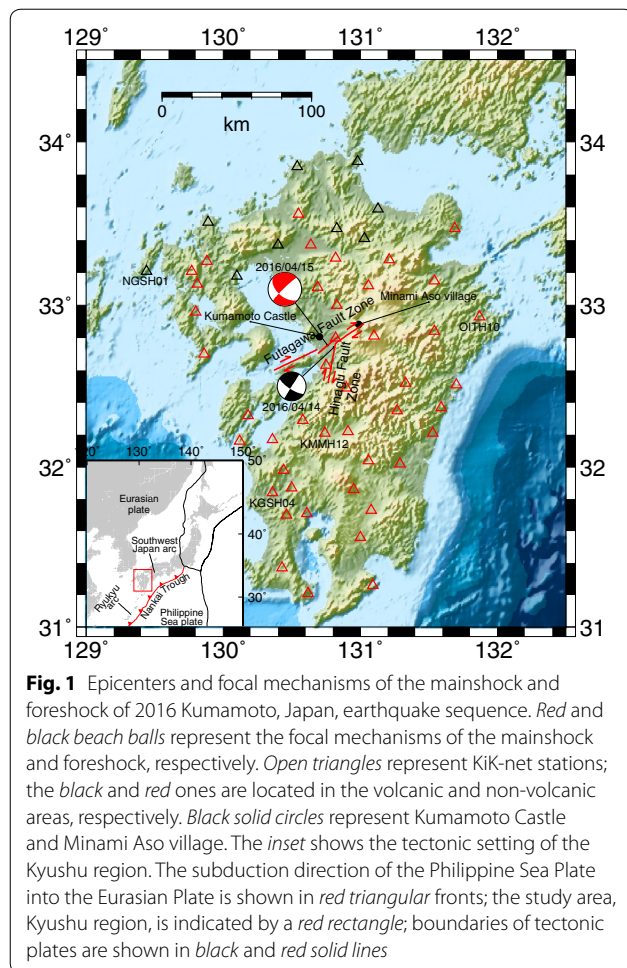
At 16:25 on April 15, 2016 (UTC), a large shallow crustal earthquake (M_w 7.1) occurred beneath Kumamoto city in the Kyushu region, Japan. Prior to the mainshock, a moderate foreshock (M_w 6.1) at 21:26 on April 14, 2016 (UTC), struck the same region. According to F-net (full range seismograph network of Japan) moment tensor solution, the hypocenters of the mainshock and foreshock were located, respectively, in the Futagawa and Hinagu fault zones, two active right-lateral strike-slip faults in the Kyushu region (Fig. 1). There were more than 1000 aftershocks with an intensity above one degree within the vicinity of Kumamoto prefecture. Peak ground acceleration (PGA) reached as high as 1362 cm/s^2 at

station KMM16 with an epicentral distance of 2 km. The strong ground motions of the 2016 Kumamoto earthquake sequence caused at least 110 fatalities and more than 2400 injuries. Numerous buildings were damaged seriously, and even collapsed, during this earthquake sequence. In particular, Kumamoto Castle, one of the most popular tourist destinations in Kumamoto prefecture, suffered destructive damage to roofs and stone walls. In addition, numerous landslides were triggered throughout the nearby mountainous areas in the Kyushu region. For example, Great Aso Bridge in Minami Aso village was swept away by a landslide and collapsed into the river. Although two dense strong-motion seismograph networks (K-NET and KiK-net) are installed and operated in Japan, some heavily damaged regions still lack strong-motion stations. Ground-motion simulations for the 2016 Kumamoto earthquake have important implications, not only for seismic hazard assessment, such as

*Correspondence: zhanglong98524@163.com

¹ Department of Civil and Structural Engineering, Kyushu University, Fukuoka 819-0395, Japan

Full list of author information is available at the end of the article



slope stability analysis and landslide run-out estimation, but for earthquake-resistant design, such as response spectrum analysis of structures in the damaged regions.

In this paper, the ground-motion simulations for the 2016 Kumamoto earthquake have been performed using the stochastic finite-fault method based on a dynamic corner frequency. Our major objectives are to determine region-specific source, path and site parameters, to validate our finite-fault model and to simulate ground motions in severely damaged areas that do not have strong-motion stations. For these purposes, we first determined input parameters including quality factor (Q_s), zero-distance kappa (κ_0), which represents the effect of rapid spectral decay at high frequencies, site amplifications in the Kyushu region and the stress drop of the mainshock. Then, the ground-motion simulations were performed and compared with the observations at all stations. Simulated PGA values were also compared with ground-motion prediction equations (GMPEs) suggested by Boore et al. (2014). Finally, we performed blind

simulations for Kumamoto Castle and Minami Aso village based on our validated model, where engineered structures suffered severe damages but without ground-motion records.

Methods

The stochastic finite-fault method is widely used in ground-motion simulations of past or scenario earthquakes (Ugurhan and Askan 2010; Ghofrani et al. 2013; Safarshahi et al. 2013; Zengin and Cakti 2014; Mittal and Kumar 2015). Compared with other ground-motion simulation methods, such as the deterministic or hybrid approach, the advantages of the stochastic method are its independence of small earthquake selection and good performance at both low and high frequencies (Motazedian and Atkinson 2005). In this method, near-field ground motions, including the acceleration time series, Fourier amplitude spectra (FAS) and 5%-damped pseudo-acceleration response spectra (PSAs), can be synthesized at the frequency range of engineering interest (Atkinson et al. 2009). In particular, the 5%-damped PSA represents the maximum acceleration caused by a linear oscillator with 5% damping and a specified natural period. In this study, we employ the latest version of the finite-fault code EXSIM12 to simulate the ground motions of the 2016 Kumamoto earthquake. For each station, we simulate surface recordings with ten trials to eliminate the bias resulting from stochastic variability.

Data and processing

We employ strong ground-motion records from the KiK-net borehole and surface seismic network for the 2016 Kumamoto earthquake. A total of 53 KiK-net stations in the Kyushu region recorded this event (Table 1). The quality of each record from these stations is evaluated based on the signal-to-noise ratio (SNR) technique suggested by Ktenidou et al. (2011). All records are proved to be high quality as they pass the strict selection criterion of a SNR threshold of 3. Borehole recordings are used to compute the Q_s beneath the volcanic area, whereas surface recordings are used to estimate κ . Site amplification at each station is calculated using the horizontal-component (N–S and E–W) borehole and surface recordings.

Preliminary data processing is implemented for each record. First, we employ the empirical approach with an automatic scheme (Wang et al. 2011) to correct baseline for raw data. The corrected records are band-pass filtered in the frequency range of 0.1–25 Hz with a fourth-order Butterworth filter. Second, the S -wave and noise windows are extracted and tapered at both ends with a 10% Hanning-type window. Finally, FAS are computed for both S -wave and noise windows.

Table 1 Information on the strong-motion stations used in this study

Station code	Latitude (°N)	Longitude (°E)	Epicentral distance (km)	PGA (cm/s ²)	V ₃₃₀ (m/s)
<i>FKOH01</i>	33.8849	130.9798	121	60	588.5
<i>FKOH03</i>	33.5608	130.5499	88	135	497.0
<i>FKOH06</i>	33.5925	131.1348	93	75	1001.8
<i>FKOH07</i>	33.3678	130.6354	65	94	282.9
<i>FKOH08</i>	33.4654	130.8285	74	103	535.8
<i>FKOH09</i>	33.8501	130.5432	119	43	566.7
<i>FKOH10</i>	33.2891	130.817	54	89	921.3
<i>KGSH01</i>	32.1554	130.1191	96	49	603.0
<i>KGSH03</i>	31.9812	130.4438	97	37	1196.2
<i>KGSH04</i>	31.8374	130.3602	114	41	280.4
<i>KGSH05</i>	31.8699	130.4958	107	74	477.5
<i>KGSH06</i>	31.6988	130.4594	126	30	454.9
<i>KGSH07</i>	31.714	130.6149	122	47	260.0
<i>KGSH08</i>	31.5618	130.9969	138	10	–
<i>KGSH09</i>	31.3741	130.4333	162	13	409.1
<i>KGSH10</i>	31.2066	130.6183	177	6	254.9
<i>KGSH12</i>	31.2583	131.0877	173	3	451.6
<i>KMMH01</i>	33.1089	130.6949	36	252	574.6
<i>KMMH02</i>	33.122	131.0629	43	687	576.7
<i>KMMH03</i>	32.9984	130.8301	22	800	421.2
<i>KMMH06</i>	32.8114	131.101	28	180	567.8
<i>KMMH09</i>	32.4901	130.9046	36	246	399.7
<i>KMMH10</i>	32.3151	130.1811	79	195	176.9
<i>KMMH11</i>	32.2918	130.5777	60	88	1292.3
<i>KMMH12</i>	32.2054	130.7371	66	218	409.8
<i>KMMH13</i>	32.2209	130.9096	65	113	402.5
<i>KMMH14</i>	32.6345	130.7521	19	612	248.3
<i>KMMH15</i>	32.1704	130.3647	81	76	499.9
<i>KMMH16</i>	32.7967	130.8199	2	1362	279.7
<i>MYZH04</i>	32.5181	131.3349	83	175	484.4
<i>MYZH05</i>	32.347	131.2668	59	142	1072.5
<i>MYZH08</i>	32.2132	131.5309	67	143	374.4
<i>MYZH09</i>	32.0421	131.0618	95	17	973.0
<i>MYZH10</i>	32.0215	131.29	88	98	494.7
<i>MYZH12</i>	31.8643	130.9454	98	96	319.5
<i>MYZH13</i>	31.7301	131.0791	105	50	251.2
<i>MYZH15</i>	32.3654	131.5893	121	118	445.7
<i>MYZH16</i>	32.506	131.6958	88	45	847.5
<i>NGSH01</i>	33.2116	129.4353	90	42	397.8
<i>NGSH02</i>	33.2122	129.7652	135	23	642.1
<i>NGSH03</i>	33.1256	129.8102	107	39	634.5
<i>NGSH04</i>	32.9553	129.8026	99	40	633.2
<i>NGSH06</i>	32.6999	129.8625	95	30	1421.1
<i>OITH01</i>	33.4122	131.0326	89	70	865.1
<i>OITH03</i>	33.4736	131.6856	71	25	486.0
<i>OITH05</i>	33.1525	131.542	111	89	1269.4
<i>OITH08</i>	32.8392	131.5357	80	86	657.4
<i>OITH10</i>	32.9278	131.8695	69	49	836.9
<i>OITH11</i>	33.2844	131.2118	101	598	458.0

Table 1 continued

Station code	Latitude (°N)	Longitude (°E)	Epicentral distance (km)	PGA (cm/s ²)	V_{330} (m/s)
<i>SAGH01</i>	33.508	129.8877	66	37	980.2
<i>SAGH02</i>	33.2656	129.8798	116	70	557.9
<i>SAGH04</i>	33.3654	130.4046	100	149	724.1
<i>SAGH05</i>	33.1806	130.1046	73	32	1000.0

The stations located in the non-volcanic area are shown in italics

Input parameters

Source parameters

Source information, such as moment magnitude, hypocenter location, fault geometry and subfault size, is required to define the source mechanism in the stochastic finite-fault model. According to the F-net moment tensor solution determined by the National Research Institute for Earth Science and Disaster Prevention (NIED), the moment magnitude of the mainshock is M_w 7.1, the hypocenter location is at 32.7545°N, 130.763°E, the focal depth is 11 km, and the strike and dip of the fault plane are 224° and 65°, respectively. The fault plane is divided into 18×9 subfaults with dimensions of 5 km \times 2.9 km along the strike and dip, following Hayes (2016)'s routine of discretization. The slip distribution (Fig. 2), which directly controls the seismic moment of each subfault, is prescribed on the basis of teleseismic waveform inversion (Hayes 2016). Some source parameters, such as density, rupture propagation velocity and pulsing area percentage, are assigned with commonly used values according to previous studies (Table 2).

S -wave velocity (V_s) anomalies are taken into account in this paper. Some studies (e.g., Zhao et al. 2011; Liu and Zhao 2016) report that low-velocity zones exist beneath

the volcanic areas in the Kyushu region. For example, Zhao et al. (2011) revealed a -3% V_s perturbation at a depth of 5–15 km under active volcanic areas in the Kyushu region using tomography method. In this study, we assume the V_s is 3.6 and 3.7 km/s beneath the volcanic and non-volcanic areas, respectively, as constrained by the tomographic results (Zhao et al. 2011) and typical crustal V_s profiles (Atkinson and Boore 2006).

We determine the stress drop using an optimization algorithm. It follows the criterion of minimizing the average absolute residual of observed and simulated PSA in terms of common logarithmic form (Ghofrani et al. 2013). The residual is defined as

$$\text{res}(f, R_{JB}) = \log_{10}(\text{PSA}_{\text{obs}}) - \log_{10}(\text{PSA}_{\text{sim}}), \quad (1)$$

where f is the frequency of ground motion and R_{JB} is the closest horizontal distance to the surface projection of the fault plane (Kaklamanos et al. 2011). The average absolute residual is defined as

$$|\overline{\text{res}}| = \frac{1}{N_f N_d} \sum_{n=1}^{N_f} \sum_{m=1}^{N_d} |\text{res}(f, R_{JB})|, \quad (2)$$

where N_f and N_d are the number of frequencies and distances, respectively.

Path parameters

In the stochastic finite-fault method, the path spectrum, $G(R) \exp[-\pi f R / \beta Q_s(f)]$, depends on geometrical spreading ($G(R)$) and quality factor (Q_s). For the geometrical spreading, we use a popular piecewise function expressed in the following form (Zengin and Cakti 2014),

$$G(R) = \begin{cases} R^{-1}, & R < 100 \text{ km} \\ (100R)^{-0.5}, & R \geq 100 \text{ km} \end{cases}. \quad (3)$$

One objective of this study is to make a reliable estimate of Q_s in the Kyushu region. The quality factor, Q_s , is an indicator of regional S -wave anelastic attenuation. Aki and Chouet (1975) suggested a power-law form of $Q_s = Q_0 f^\eta$, where Q_0 is the value of Q_s at a frequency of 1 Hz and η is the frequency parameter. We use a classical spectral decay method (Anderson and Quaaas 1988) to determine it as follows. The FAS recorded at hypocentral distance R , $U(f, R)$, can be expressed as

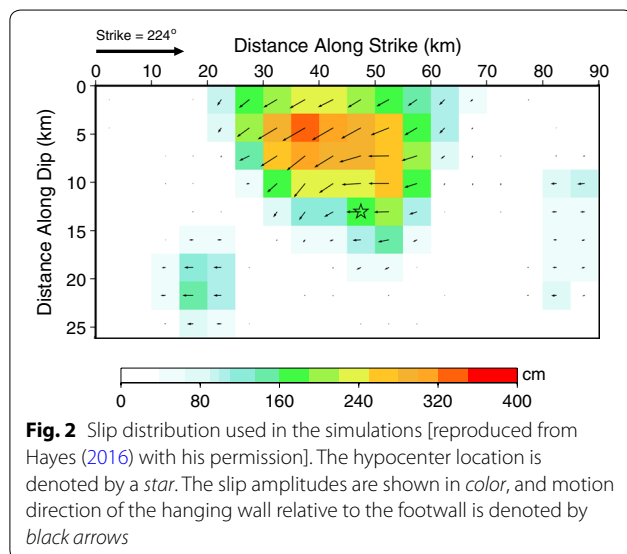


Table 2 Input parameters for the stochastic finite-fault model of the 2016 Kumamoto earthquake

Parameters	Value	Reference
<i>Source</i>		
Moment magnitude (M_w)	7.1	F-net
Hypocenter location	32.754°N, 130.763°E, 11 km	F-net
Strike and dip angle (°)	224 and 65	F-net
Subfault length and width (km)	5 and 2.9	Hayes (2016)
Slip distribution	Prescribed	Hayes (2016)
Stress drop (bars)	64	This study
S-wave velocity (km/s)	3.6 (beneath the volcanic areas) 3.7 (beneath the non-volcanic areas)	Estimated from Zhao et al. (2011), Atkinson and Boore (2006)
Density (g/cm ³)	2.8	Atkinson et al. (2009)
Rupture propagation velocity	0.8 β	Atkinson and Boore (2006)
Pulsing area percentage	50%	Atkinson and Boore (2006)
<i>Path</i>		
Geometric spreading, R^b : $b=$	-1.0 (0–100 km) -0.5 (>100 km)	Zengin and Cakti (2014)
Ground-motion duration, dR , $d=$	0.0 (0–10 km) +0.16 (10–70 km) -0.03 (70–130 km) +0.04 (>130 km)	Atkinson and Boore (1995)
Quality factor	$Q_s = (85.5 \pm 1.5)f^{0.68 \pm 0.01}$ (beneath the volcanic areas) $Q_s = (120 \pm 5)f^{0.64 \pm 0.05}$ (beneath the non-volcanic areas)	This study
<i>Site</i>		
Site amplification	See Additional files	This study
κ (s)	0.0514 \pm 0.0055	This study

$$U(f, R) = S \cdot G(R) \exp(-\pi f R / \beta Q_s), \quad (4)$$

where S is a source-dependent scalar. Equation (4) can be shown in a linear relationship by using natural logarithm on both sides,

$$\ln(U(f, R)/G(R)) = -\frac{\pi f}{\beta Q_s} R + \ln(S). \quad (5)$$

For a given frequency, the Q_s^{-1} and its standard error can be calculated from the slope of Eq. (5) with an assumed S -wave velocity (β). The corrected FAS of each horizontal component [the left hand of Eq. (5)] are plotted against hypocentral distance at the frequency range of 1–25 Hz with 1-Hz spacing. We average Q_s^{-1} of N–S and E–W components at each frequency and plot them against the frequency range (Fig. 3). The Q_s^{-1} can be obtained by using standard linear regression.

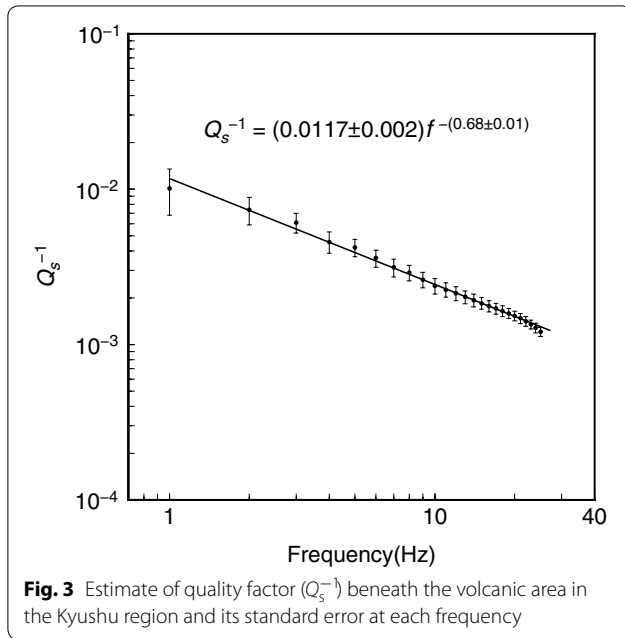
Significant lateral Q_s heterogeneities in the Kyushu region have been reported by many studies. Low- Q anomalies are revealed by tomography method in the crust and uppermost mantle beneath active volcanic areas, such as Aso, Sakurajima and Kirishima, whereas the subducting Philippine Sea slab exhibits high- Q character (e.g., Pei et al. 2009; Liu and Zhao 2015). Given the strong lateral Q_s variations in the Kyushu region, we

divide all stations into volcanic area stations and non-volcanic area stations (shown in Fig. 1; Table 1). The Q_s beneath the volcanic area is estimated from the borehole recordings of 44 stations located in the volcanic areas, based on Liu and Zhao (2015)'s tomographic results [Fig. S29(a) of their work]. However, the number of stations in the non-volcanic area (9) is inadequate to provide a robust estimate of Q_s . Therefore, we choose to estimate the non-volcanic area Q_s by combining the volcanic area Q_s and Q_s perturbation identified from Fig. S29(a) of Liu and Zhao (2015). Specifically, the non-volcanic area Q_0 equals to the volcanic area Q_0 divided by 1 plus the Q_s perturbation. For η , we use Oth et al. (2011)'s estimate for the Kyushu region. In addition, we also calculate Q_s using all stations to investigate the effect of lateral Q_s variations on ground-motion simulations.

Ground-motion duration is another important path parameter to trigger seismic hazards, such as liquefaction. We use a well-known distance-dependent duration model obtained by Atkinson and Boore (1995).

Site effects

Site amplifications and κ_0 are two parameters required to characterize the site response in the stochastic finite-fault method. A corrected cross-spectral ratio technique



is used to compute site amplification at each station as follows:

$$S/B' = \frac{|S_{12}(f)|^2}{S_{11}(f)S_{22}(f)} (S/B), \quad (6)$$

where $S_{11}(f)$ and $S_{22}(f)$ are the power spectral densities of the surface and borehole recordings, respectively, $S_{12}(f)$ is the cross-power-spectral density function and S/B refers to the ratio of surface FAS over borehole FAS at a certain station. Note that all variables in Eq. (6) are the geometric mean of two horizontal components smoothed with a Konno–Ohmachi filter (Konno and Ohmachi 1998).

Additionally, kappa filter (κ) is adopted to represent the slope of high-frequency decay of FAS in the stochastic finite-fault method. A model (Anderson and Hough 1984) characterized the shape of FAS at high frequencies, shown as

$$a(f) = A_0 \exp(-\pi\kappa f) \quad \text{for } f > f_e, \quad (7)$$

where A_0 is a source and propagation path-dependent amplitude and f_e is the lower cutoff frequency above which the decay of FAS can be considered as approximately linear observed in a log-linear space. κ can be calculated from the slope λ of FAS over a certain frequency range (Δf) in a log-linear space:

$$\kappa = -\lambda/\pi, \quad (8)$$

where $\lambda = \Delta(\ln a)/\Delta f$. The distance dependence of κ was also observed and suggested by Anderson and Hough (1984) in the linear form of

$$\kappa = \kappa_0 + \kappa_R R, \quad (9)$$

where κ_0 is the zero-distance kappa, κ_R is the slope and R is the epicentral distance. We use the classic routine (Anderson and Hough 1984) mentioned above to determine κ for each horizontal-component record. At each station, we average two horizontal-component κ values and consider it to be the representative. κ_0 [the intercept of Eq. (9)] is determined by extrapolating the κ values to $R = 0$.

Our optimized finite-fault model consists of the source, path and site parameters. They are summarized in Table 2.

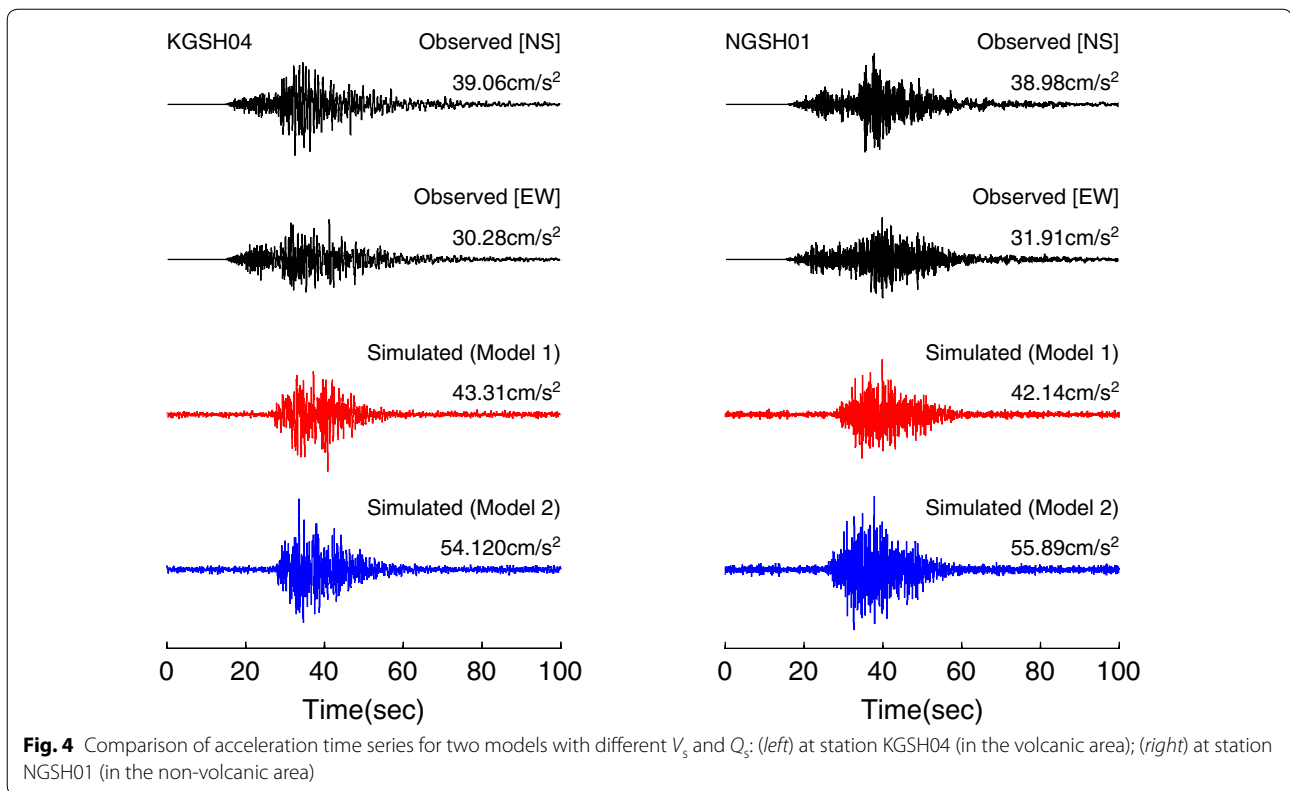
Results and discussion

Region-specific parameters

Region-specific parameters are determined in this paper, including the quality factor (Q_s), zero-distance kappa (κ_0), site amplifications and the stress drop of the mainshock.

We determine the frequency-dependent Q_s in the Kyushu region by incorporating lateral variations. The Q_s^{-1} beneath the volcanic area is estimated and expressed in the form of $Q_s^{-1} = (0.0117 \pm 0.002)f^{-(0.68 \pm 0.01)}$ (Fig. 3). In the simulations, it is transformed to $Q_s = (85.5 \pm 1.5)f^{0.68 \pm 0.01}$. It is in good agreement with Oth et al. (2011)'s result, $Q_s = (91 \pm 8)f^{0.64 \pm 0.05}$, which is derived from a non-parametric spectral inversion scheme and based on a much richer dataset. Additionally, Q_s beneath the non-volcanic area is also estimated and shown in the form of $Q_s = (120 \pm 5)f^{0.64 \pm 0.05}$. Both Q_0 are consistent with the results of an S -wave attenuation tomography performed by Pei et al. (2009). Therefore, the Q_s we estimated provides a convincing proof to describe the complexity of crustal structure in the Kyushu region. In addition, we also obtain the Q_s without considering lateral variations in the form of $Q_s = (102 \pm 5)f^{0.67 \pm 0.01}$.

Further, the effect of lateral V_s and Q_s heterogeneities on the ground-motion simulations is investigated. The finite-fault models with and without the lateral V_s and Q_s heterogeneities are referred to as Model 1 and Model 2, respectively. Ground-motion simulations at all stations are performed with both of them. We select two representative stations to highlight their differences. Station KGSH04 is located near Sakurajima, which is one of seven active volcanoes in the Kyushu region. Station NGSH01 is located in the non-volcanic area. The differences between two models in simulation results are shown in Figs. 4, 5 and 6. In the time domain (Fig. 4), the observed and simulated acceleration time series show good agreement at both stations, but the simulated PGAs of Model 1 are closer to the observed ones. Similarly, in the frequency domain (Figs. 5, 6), Model 1



behaves better than Model 2 in terms of FAS, PSA and their residuals at high frequencies (frequency >1 Hz) or short periods (period <1 s). The differences between two simulation results mainly rise from significantly different values of Q_s at high frequencies. Therefore, it indicates that lateral V_s and Q_s heterogeneities can affect the simulation results in both the time and frequency domains. In the next section, we present and discuss the simulation results based on Model 1.

κ_0 is estimated to be 0.0514 ± 0.0055 s (Fig. 7). Such a high value corresponds to soft rock sites or unstable regions, where high-frequency energy is rarely observed (Ktenidou et al. 2014). In Table 1, 74% of the stations in the Kyushu region are located in class C (soft rock, $V_{S30} = 360\text{--}760$ m/s) and D (stiff soil, $V_{S30} = 180\text{--}360$ m/s) sites based on the National Earthquake Hazards Reduction Program (NEHRP) site classes using V_{S30} as the most important parameter for site classification, where V_{S30} represents the time-weighted average S -wave velocity over the upper 30 m of the profile (Boore et al. 2014). Thus, the soil conditions in the Kyushu region may result in a high κ_0 . The second possible reason is the active tectonic setting. Considerable volcanic activities associated with low-frequency microearthquakes occur in the Kyushu region. Therefore, such an active tectonic

(unstable) region may be consistent with a high κ_0 . An important application of κ_0 is that it can be used as a low-pass filter to constrain high frequencies, influencing PGA and spectral level in the generation of ground motions when using stochastic method or hybrid method (Ktenidou et al. 2014). Moreover, κ_0 has been included in the functional form of GMPEs explicitly to characterize site attenuation that dominates high frequencies. In summary, the well-determined κ_0 in the Kyushu region contributes to the generation of reliable synthetic ground motions and to the calibration of GMPEs in engineering seismology.

Site amplification in the Kyushu region is estimated by using the corrected cross-spectral ratios technique (see Additional file 1: Figure S1). Compared with the classic standard spectral ratio technique, the “depth effect” reported by Cadet et al. (2012) is corrected. The amplified waves usually lead to destructive damage to engineered structures at the surface. Therefore, a calibrated estimate of the site response in the target region is essential not only for ground-motion simulations, but for site classification, both of which are necessary for the earthquake-resistant design of engineered structures.

The stress drop based on the USGS slip model (Hayes 2016) is calculated by minimizing the average absolute

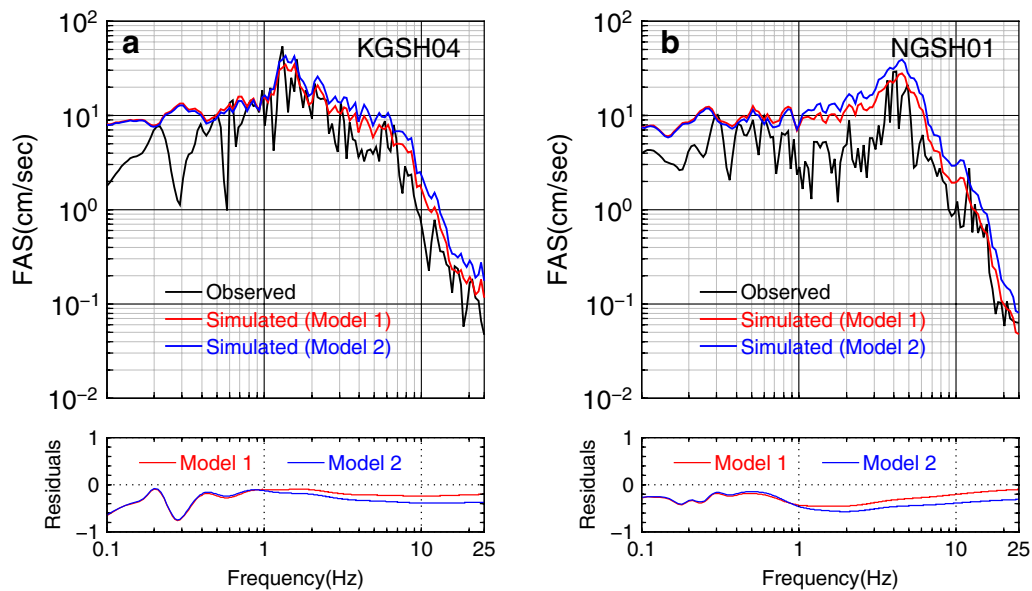


Fig. 5 Comparison of FAS and their residuals for two models with different V_s and Q_s : **a** at station KGSH04 (in the volcanic area), **b** at station NGSH01 (in the non-volcanic area)

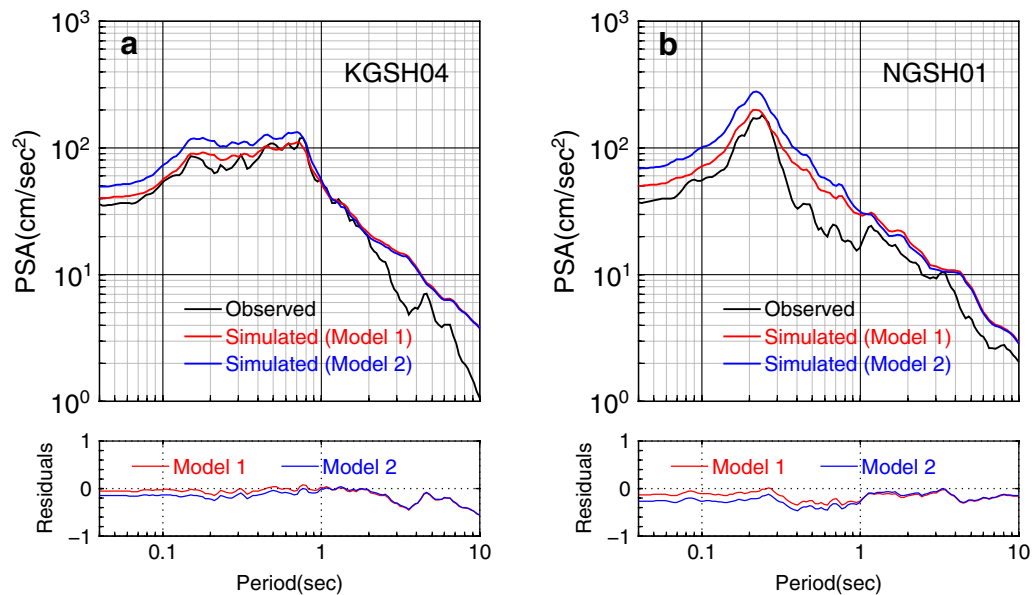
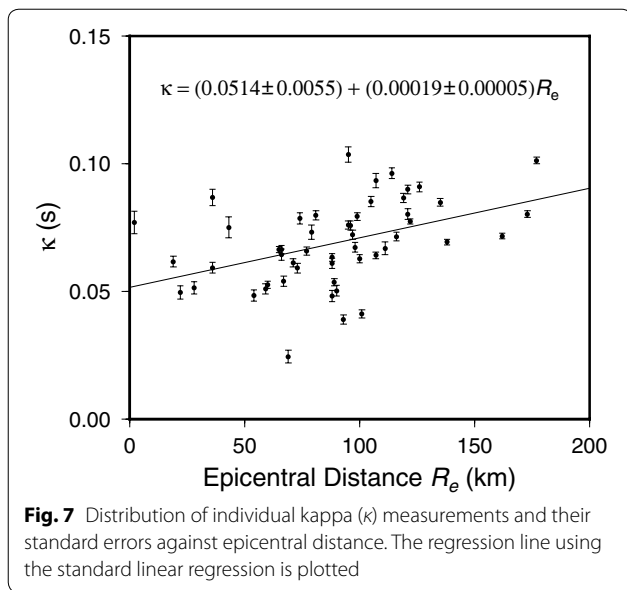


Fig. 6 Comparison of PSAs and their residuals for two models with different V_s and Q_s : **a** at station KGSH04 (in the volcanic area), **b** at station NGSH01 (in the non-volcanic area)

residual of observed and simulated PSAs. The optimized value of stress drop, 64 bars, is reasonable for a large event (Ugurhan and Askan 2010; Zengin and Cakti 2014). The stress drop determined here contributes to reliable estimates of simulated PSA, because it controls the spectral amplitude at high frequencies (Motazedian and Atkinson 2005).

Model validation

Our finite-fault model using optimized parameters is validated by comparison between the observed and simulated acceleration time series, FAS and 5%-damped PSAs at all stations. To validate the attenuation characteristics of PGAs against distance, GMPEs suggested by Boore et al. (2014) are used. Moreover, the simulated PGAs are

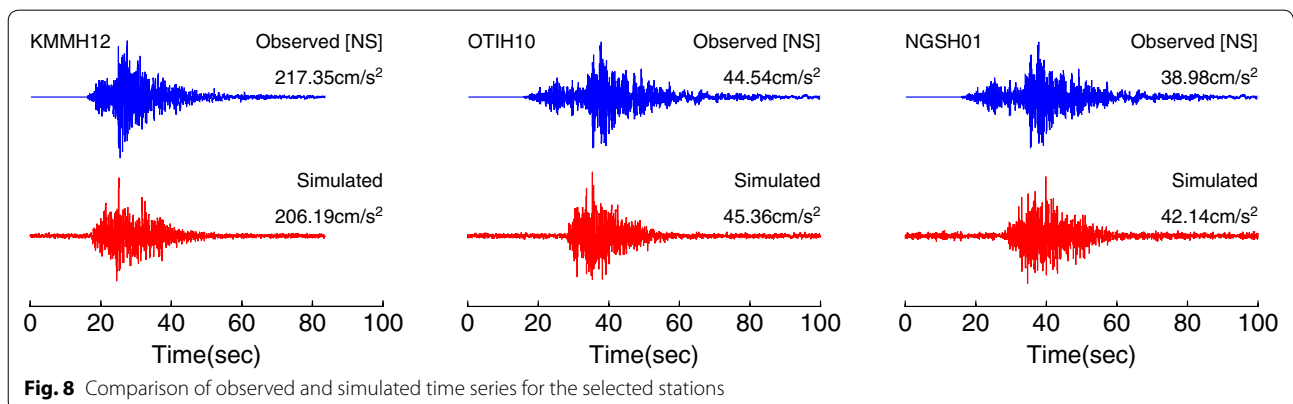


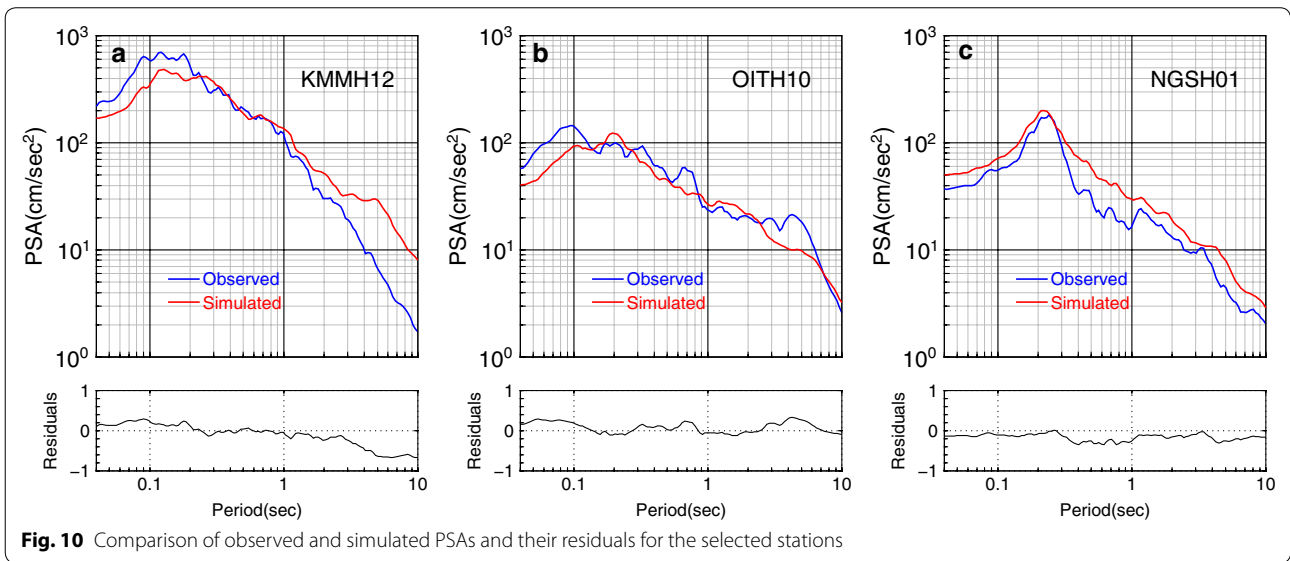
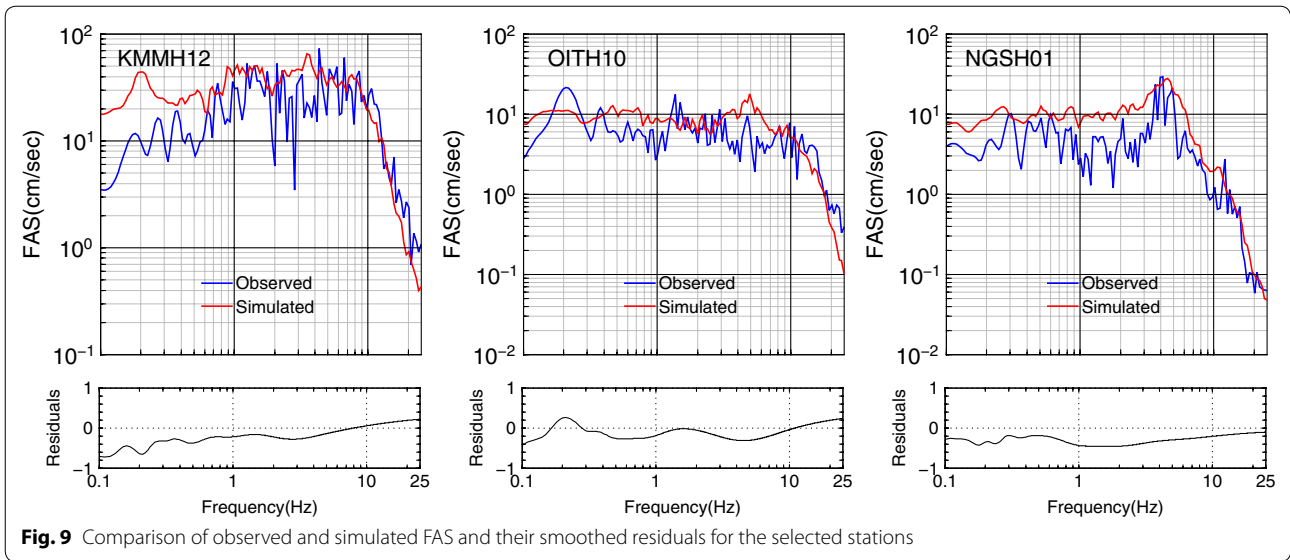
also compared with the observations in regional scale. Note that we use horizontal-component geometric mean at the surface as observed ground-motion variables (i.e., FAS and 5%-damped PSA), whereas the simulated ones are the averages of ten trials. For synthetic acceleration time series, we select the one with its peak value closest to the average of ten trials. Comparison of observed and simulated time series, FAS and PSAs at all stations can be found in the Additional files (see Additional files 2: Figure S2, 3: Figure S3, 4: Figure S4). To avoid lengthy comparisons, we select one station at each epicentral distance range of 0–50, 50–100 and larger than 100 km, respectively, for further discussion.

Figure 8 shows the results of observed and simulated acceleration time series at selected stations. In the time domain, the envelopes of the synthetic acceleration time series are very similar to the real ones. It indicates that the observed and simulated acceleration time series match very well.

Figure 9 shows the observed and simulated 5%-damped PSAs and their residuals at selected stations. To quantify the misfit, we calculate the smoothed FAS residuals using Eq. (1) (replacing the PSA with FAS). The maximum absolute residual at high frequencies is as low as 0.45, whereas at low frequencies it is 0.71. The lower value of residual means better agreement of observations and simulations. Thus, the simulated FAS at high frequencies match well with the observed ones, but are overestimated at low frequencies. The good agreement of FAS at high frequencies rises from the exact estimate of the high-frequency cut-off filter, κ_0 . The misfit of FAS at low frequencies might be attributed to the uncertainty of the slip distribution. The source spectrum increases as $CM_{0ij}H_{ij}(2\pi f)^2$ (Motazedian and Atkinson 2005). The moment magnitude of each subfault, M_{0ij} is assigned as $M_0S_{ij}/\sum_{i=1}^n\sum_{j=1}^n S_{ij}$ where S_{ij} is the relative slip weight of the ij th subfault. The spectral amplitude at low frequencies is more sensitive to the slip distribution, because the effect of the decay term $\exp(-\pi f\kappa)$ is not remarkable.

Figure 10 displays the observed and simulated 5%-damped PSAs and their residuals at selected stations. Note that the PSA residuals are calculated from Eq. (1). The maximum absolute residual at short periods is only 0.35, whereas at long periods it is 0.67. It indicates that the simulated PSAs match the observed ones better at short periods (high frequencies) than that at long periods (low frequencies). It also means the optimized value of the stress drop, 64 bars, is a reliable estimate for the mainshock of the 2016 Kumamoto earthquake, because the stress drop controls the spectral amplitude of high-frequency part (Motazedian and Atkinson 2005). Note that the stress drop is model dependent (Atkinson et al. 2009). If another slip model is applied, the optimized value of the stress drop will be expected to change. The slight misfit of PSA observed at long periods is partly due to the pulsing area percentage. It is reported that a large pulsing area will boost the amplitudes at longer periods and higher energy radiation (Motazedian and



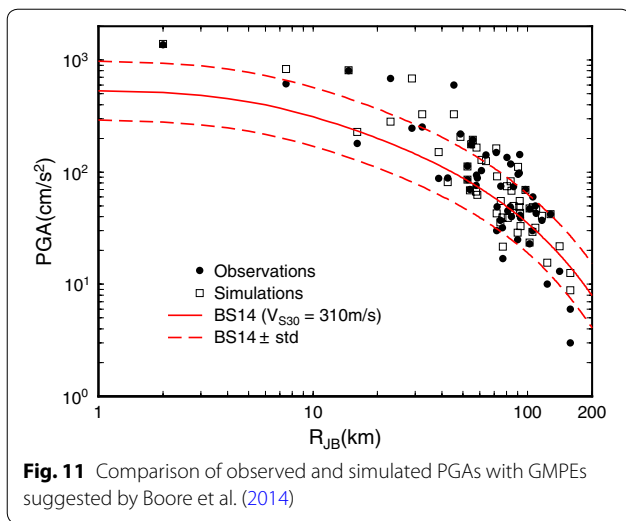


Atkinson 2005). The performance of PSA at long periods can be improved by altering the pulsing area. However, strict selection of the pulsing area is beyond the scope of this paper. On the basis of the rule of thumb, we select the commonly used 50% as the value of pulsing area percentage.

For further validation, observed and simulated PGAs at all station are compared with GMPEs derived from NGA-West2 database (Fig. 11). For the observed PGAs, we use the composite maximum acceleration of three-component records. For the simulated ones, we use the one closest to the average of ten trials. The median trend

of GMPEs is plotted as a function of R_{JB} , for a strike-slip earthquake and a generic soil site with $V_{S30} = 310$ m/s. In Fig. 11, most of the individual PGAs fall in the region between the upper and lower limits of one standard deviation. It indicates that the attenuation characteristics of the simulated PGAs are also captured well by the GMPEs.

We then plotted the observed and simulated PGA contour maps in regional scale (Fig. 12). Higher values are expected to concentrate around the epicenter and distributed along the motion direction of the strike-slip faults (NE–SW). The severely damaged regions,



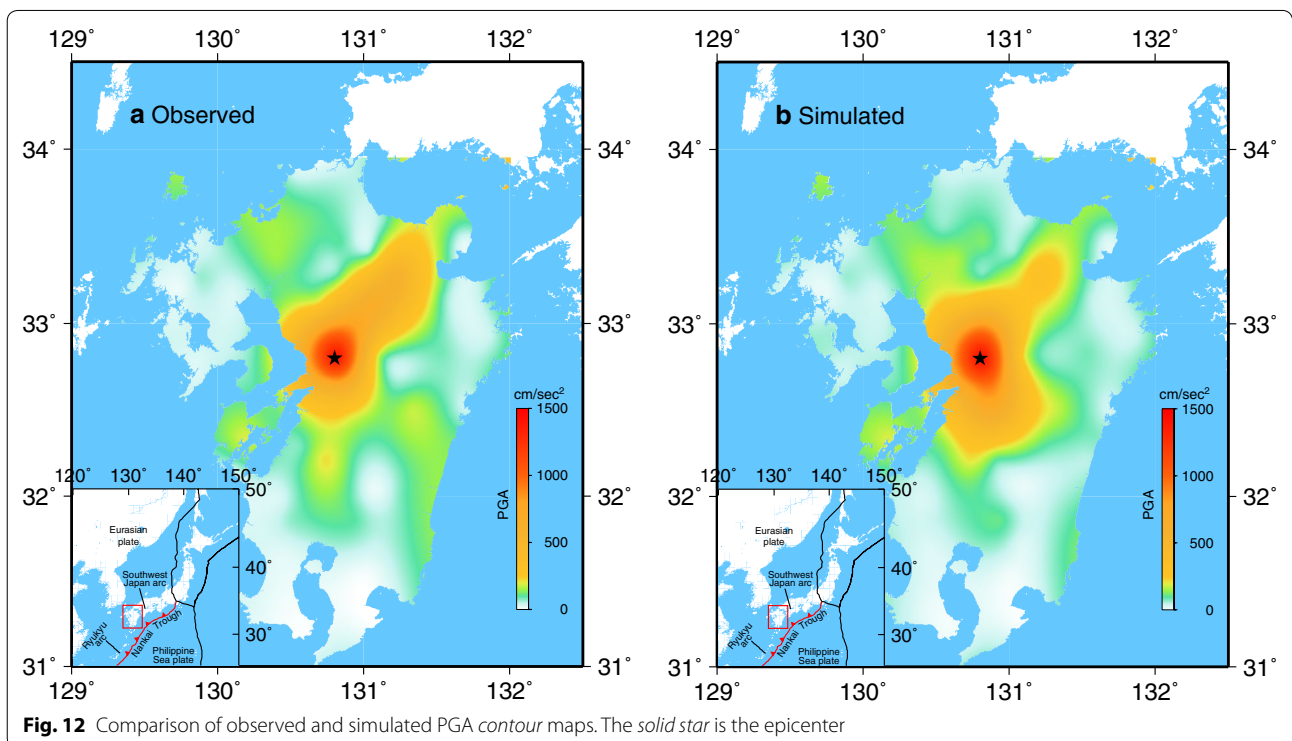
with intensity above 5°, locate in the vicinity of Kumamoto prefecture, which is mostly overlapped by simulated high-PGA regions. The underestimation observed in the northeastern region can be attributed to the slip heterogeneity on the fault plane, because the details of slip distribution, such as the locations and slip amounts of asperities, have a significant effect on the near-field

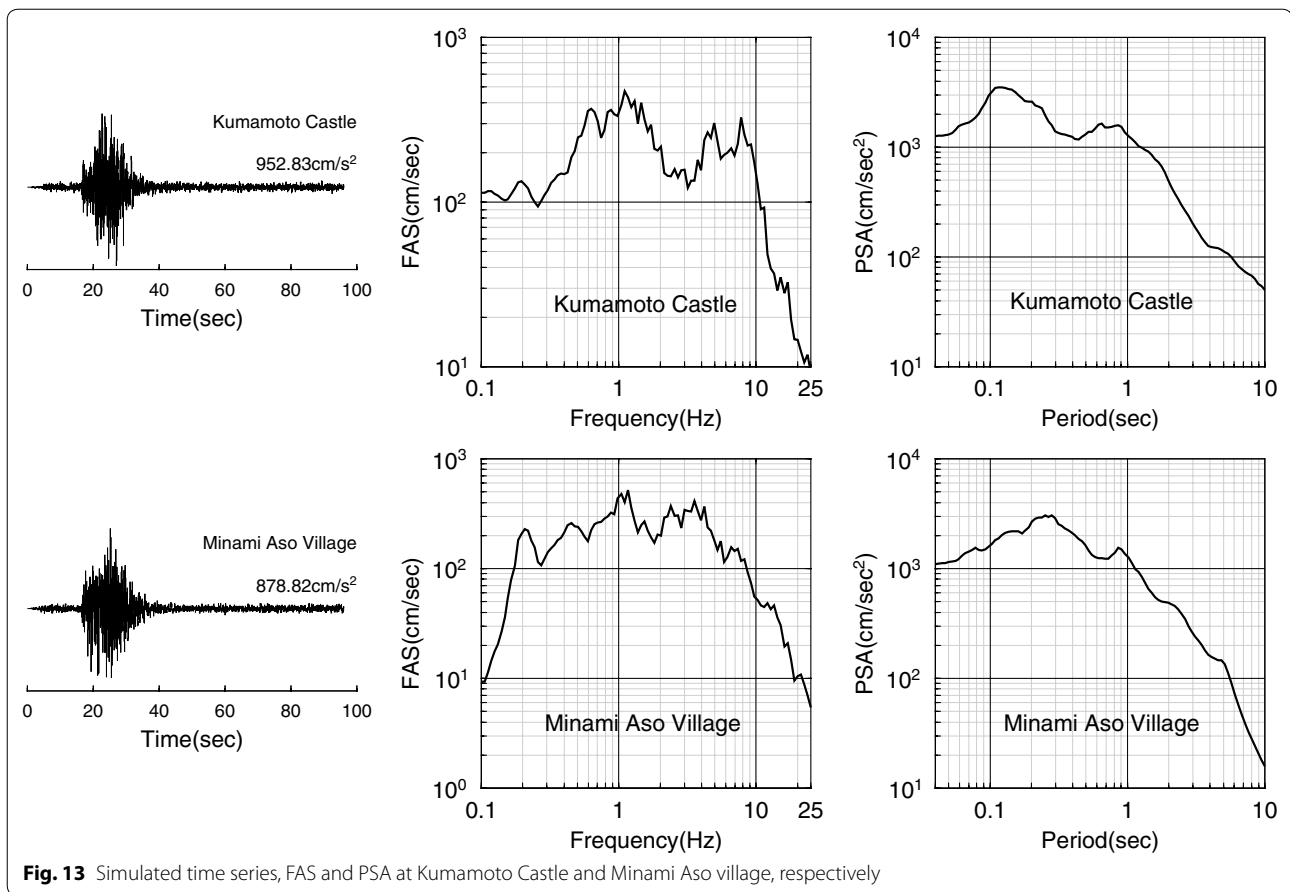
ground-motion distribution at the surface (Zengin and Cakti 2014). Nevertheless, the simulated PGA distribution in the Kyushu region shows an overall good agreement with the observed one.

Our finite-fault model with optimal parameters is validated well through the good agreement of observations and simulations in both the time and frequency domains at all stations. It shows the capacity to perform ground-motion simulations at some critical but not-instrumented sites.

Blind simulations

We then simulate the ground motions of Kumamoto Castle and Minami Aso village caused by the main-shock, which suffered destructive damage. As the site amplifications are unknown, we assign those of KMMH06 and KMMH14 as alternatives based on their V_{S30} (close to the representatives of the NEHRP class C and D sites) and relative distance to the targets. The simulation results based on our optimized model are shown in Fig. 13. The simulated PSA at Kumamoto Castle can be applied to the response spectrum analysis. Similarly, the simulated acceleration time series at Minami Aso village has applications for seismic hazard analysis, such as slope stability analysis or landslide run-out estimation.





Conclusions

The 2016 Kumamoto earthquake caused severe casualty and building damage. Investigating the ground-motion characteristics of this earthquake is essential for seismic hazard analysis and earthquake-resistant design. In this study, we use the stochastic finite-fault method based on a dynamic corner frequency to simulate the strong ground motions of the 2016 Kumamoto earthquake.

To achieve realistic simulation results, the source, path and site parameters in the Kyushu region are calibrated. For source effect, the stress drop of the mainshock is determined to capture the characteristics of high-frequency response spectrum, with an optimized value of 64 bars. For path effect, the low- Q anomalies beneath the volcanic area are revealed by frequency-dependent attenuation relation $Q_s = (85.5 \pm 1.5)f^{0.68 \pm 0.1}$. Besides, the S -wave attenuation beneath the non-volcanic area is also estimated and expressed as $Q_s = (120 \pm 5)f^{0.64 \pm 0.05}$. For site response, κ_0 with a value of 0.0514 ± 0.0055 s in the Kyushu region characterizes linear decay trend of FAS at high frequencies accurately, contributing to PGA, spectral level of ground motions and the calibration of GMPEs in engineering seismology. In addition, site

amplifications in the Kyushu region are also estimated to quantify impedance effect, while seismic waves traverse soil layers near the surface, which is necessary for ground-motion simulations and site classification. Overall, the calibration of region-specific parameters contributes to reliable ground-motion simulations.

In conclusion, the stochastic finite-fault method based on a dynamic corner frequency is able to reproduce the ground-motion characteristics of the 2016 Kumamoto earthquake. Our finite-fault model is validated by the comparison of observations and simulations at all stations and regional scale, which shows good agreements in both the time and frequency domains. Attenuation characteristics of the simulated PGAs are also captured well by the GMPEs. Finally, we simulate the ground motions for two severely damaged regions, Kumamoto Castle and Minami Aso village, with the validated model. The simulation results can be further considered as an input for slope stability analysis, landslide run-out estimation and response spectrum analysis of structures. This work provides a deep insight into seismic hazard assessment and mitigation in the Kyushu region, Japan.

Additional files

Additional file 1: Figure S1. Site amplifications at all stations.

Additional file 2: Figure S2. Comparison of observed and simulated acceleration time series at all stations.

Additional file 3: Figure S3. Comparison of observed and simulated FAS at all stations.

Additional file 4: Figure S4. Comparison of observed and simulated PSAs at all stations.

Authors' contributions

LZ conceived this study, ran the simulations, performed data analysis and drafted the manuscript. GC and YW revised the manuscript. HJ carried out the strong-motion data processing. All authors read and approved the final manuscript.

Author details

¹ Department of Civil and Structural Engineering, Kyushu University, Fukuoka 819-0395, Japan. ² Institute of Earthquake Science, China Earthquake Administration, Beijing 100036, China. ³ First Crust Monitoring and Application Center, China Earthquake Administration, Tianjin 300180, China. ⁴ Department of Petroleum and Geosystems Engineering, The University of Texas at Austin, Austin, TX 78731, USA.

Acknowledgements

Ground-motion data and site information were obtained from the KiK-net at <http://www.kyoshin.bosai.go.jp/>, the NIED strong-motion seismograph networks, last accessed May 1, 2016. All the figures in this paper were prepared using Generic Mapping Tools (Wessel et al. 2013). The authors would like to thank Dr. R. Wang for providing the baseline correction code. We appreciate the helpful discussions with Z. Jiang, Z. Liu, S. Zhou, W. Wang and W. Feng. In addition, the authors thank Prof. Martha Savage (the editor) and two anonymous reviewers for their helpful comments on the draft manuscript. Also, this work was financially supported by National Science Foundation of China (41474002), Grant-in-Aid for challenging Exploratory Research (Grant No. 15K12483, G. Chen) from Japan Society for the Promotion of Science and Kyushu University Interdisciplinary Programs in Education and Projects in Research Development. These financial supports are gratefully acknowledged.

Competing interests

The authors declare that they have no competing interests.

Received: 16 June 2016 Accepted: 5 November 2016

Published online: 18 November 2016

References

- Aki K, Chouet B (1975) Origin of coda waves: source, attenuation, and scattering effects. *J Geophys Res* 80:3322–3342. doi:10.1029/JB080i023p03322
- Anderson JG, Hough SE (1984) A model for the shape of the Fourier amplitude spectrum of acceleration at high frequencies. *Bull Seismol Soc Am* 74:1969–1993
- Anderson J, Quaaas R (1988) The Mexico earthquake of September 19, 1985—effect of magnitude on the character of strong ground motion: an example from the Guerrero, Mexico strong motion network. *Earthq Spectra* 4:635–646. doi:10.1193/1.1585494
- Atkinson GM, Boore DM (1995) Ground-motion relations for eastern North America. *Bull Seismol Soc Am* 85:17–30
- Atkinson GM, Boore DM (2006) Earthquake ground-motion prediction equations for eastern North America. *Bull Seismol Soc Am* 96:2181–2205. doi:10.1785/0120050245
- Atkinson GM, Assatourians K, Boore DM, Campbell K, Motazedian D (2009) A guide to differences between stochastic point-source and stochastic finite-fault simulations. *Bull Seismol Soc Am* 99:3192–3201. doi:10.1785/0120090058
- Boore DM, Stewart JP, Seyhan E, Atkinson GM (2014) NGA-West2 equations for predicting PGA, PGV, and 5% damped PSA for shallow crustal earthquakes. *Earthq Spectra* 30:1057–1085. doi:10.1193/070113EQS184M
- Cadet H, Bard PY, Adrian RM (2012) Site effect assessment using KiK-net data: part 1. A simple correction procedure for surface/downhole spectral ratios. *Bull Earthq Eng* 10:421–448. doi:10.1007/s10518-011-9283-1
- Ghofrani H, Atkinson GM, Goda K, Assatourians K (2013) Stochastic finite-fault simulations of the 2011 Tohoku, Japan, earthquake. *Bull Seismol Soc Am* 103:1307–1320. doi:10.1785/0120120228
- Hayes G (2016) Preliminary finite fault results for the Apr 15, 2016 M_w 7.0 1 km WSW of Kumamoto-shi, Japan earthquake (Version 1). <http://earthquake.usgs.gov/earthquakes/eventpage/us20005iis#finite-fault>. Accessed 1 May 2016
- Kaklamanos J, Baise LG, Boore DM (2011) Estimating unknown input parameters when implementing the NGA ground-motion prediction equations in engineering practice. *Earthq Spectra* 27:1219–1235. doi:10.1193/1.3650372
- Konno K, Ohmachi T (1998) Ground-motion characteristics estimated from spectral ratio between horizontal and vertical components of micro-tremor. *Bull Seismol Soc Am* 88:228–241
- Ktenidou O-J, Chávez-García FJ, Ptilakis KD (2011) Variance reduction and signal-to-noise ratio: reducing uncertainty in spectral ratios. *Bull Seismol Soc Am* 101:619–634. doi:10.1785/0120100036
- Ktenidou OJ, Cotton F, Abrahamson NA, Anderson JG (2014) Taxonomy of κ : a review of definitions and estimation approaches targeted to applications. *Seismol Res Lett* 85:135–146. doi:10.1785/0220130027
- Liu X, Zhao D (2015) Seismic attenuation tomography of the Southwest Japan arc: new insight into subduction dynamics. *Geophys J Int* 201:135–156. doi:10.1093/gji/ggv007
- Liu X, Zhao D (2016) P and S wave tomography of Japan subduction zone from joint inversions of local and teleseismic travel times and surface-wave data. *Phys Earth Planet Inter* 252:1–22. doi:10.1016/j.pepi.2016.01.002
- Mittal H, Kumar A (2015) Stochastic finite-fault modeling of Mw 5.4 earthquake along Uttarakhand–Nepal border. *Nat Hazards* 75:1145–1166. doi:10.1007/s11069-014-1367-1
- Motazedian D, Atkinson GM (2005) Stochastic finite-fault modeling based on a dynamic corner frequency. *Bull Seismol Soc Am* 95:995–1010. doi:10.1785/0120030207
- Oth A, Bindi D, Parolai S, Di Giacomo D (2011) Spectral analysis of K-NET and KiK-net data in Japan, part II: on attenuation characteristics, source spectra, and site response of borehole and surface stations. *Bull Seismol Soc Am* 101:667–687. doi:10.1785/0120100135
- Pei S, Cui Z, Sun Y, Toksöz MN, Rowe CA, Gao X, Zhao J, Liu H, He J, Morgan FD (2009) Structure of the upper crust in Japan from S-wave attenuation tomography. *Bull Seismol Soc Am* 99:428–434. doi:10.1785/0120080029
- Safarshahi M, Rezapour M, Hamzehloo H (2013) Stochastic finite-fault modeling of ground motion for the 2010 Rigan Earthquake, Southeastern Iran. *Bull Seismol Soc Am* 103:223–235. doi:10.1785/0120120027
- Ugurhan B, Askan A (2010) Stochastic strong ground motion simulation of the 12 November 1999 Düzce (Turkey) earthquake using a dynamic corner frequency approach. *Bull Seismol Soc Am* 100:1498–1512. doi:10.1785/0120090358
- Wang R, Schurr B, Milkereit C, Shao Z, Jin M (2011) An improved automatic scheme for empirical baseline correction of digital strong-motion records. *Bull Seismol Soc Am* 101:2029–2044. doi:10.1785/0120110039
- Wessel P, Smith WHF, Scharroo R, Luis J, Wobbe F (2013) Generic mapping tools: improved version released. *EOS Trans AGU* 94:409–410. doi:10.1002/2013EO450001
- Zengin E, Cakti E (2014) Ground motion simulations for the 23 October 2011 Van, Eastern Turkey earthquake using stochastic finite fault approach. *Bull Earthq Eng* 12:627–646. doi:10.1007/s10518-013-9527-3
- Zhao D, Wei W, Nishizono Y, Inakura H (2011) Low-frequency earthquakes and tomography in western Japan: insight into fluid and magmatic activity. *J Asian Earth Sci* 42:1381–1393. doi:10.1016/j.jseas.2011.08.003